buildings

MDPI

Article

Study on the Deterioration of Reinforced Concrete Under Stray Currents and Chloride-Ion Coupling Effects

Yongkang Ning [1,2,*], Wanqing Zhou [1,2] and Liangcheng Wang [1,2]

[1] College of Civil Engineering and Architecture, China Three Gorges University, Yichang 443002, China; zhouwq1978@163.com (W.Z.); 202308010021004@ctgu.edu.cn (L.W.)
[2] Hubei Key Laboratory of Disaster Prevention and Mitigation, China Three Gorges University, Yichang 443002, China
* Correspondence: 202108140021012@ctgu.edu.cn

Abstract

This study examined the combined effects of chloride ions and stray DC on reinforced concrete (RC) using electromigration and impressed-current methods under varying current densities (0.5, 3.0, 5.0 mA/cm^2) and chloride concentrations (50, 1350, 5500 mg/kg). Chloride was identified as the dominant deterioration factor. At 3.0 mA/cm^2, cracking times in moderate and severe chloride environments decreased by 48.75% and 52.62%, respectively, compared to mild conditions. At 0.5 mA/cm^2 in severe conditions, the corrosion rate reached 1.317% after 20, 2.75 times that in moderate conditions. Electromigration specimens showed delayed cracking but deeper chloride penetration, while impressed-current specimens exhibited pronounced strip-shaped pitting corrosion. A quadratic polynomial model predicting cracking time based on current density and chloride concentration achieved high accuracy (R^2 = 0.95, mean relative error = 7.%). Actual corrosion mass loss was lower than theoretical Faraday values, with current efficiency increasing from 0.3–0.8% to 16.5–18.1% as current density and chloride content rose. These findings highlight the synergistic effect of stray current and chloride attack, emphasizing chloride concentration's greater impact on service life. The model provides a scientific basis for RC durability design in urban rail transit and coastal engineering.

Keywords: corrosion under stray currents; chloride corrosion; corrosion of reinforced concrete; electromigration in reinforced concrete; electrically induced corrosion

Academic Editor: Ray Kai Leung Su

Received: 30 September 2025
Revised: 23 October 2025
Accepted: 27 October 2025
Published: 29 October 2025

Citation: Ning, Y.; Zhou, W.; Wang, L. Study on the Deterioration of Reinforced Concrete Under Stray Currents and Chloride-Ion Coupling Effects. *Buildings* **2025**, *15*, 3913. https://doi.org/10.3390/buildings15213913

1. Introduction

Reinforced concrete has become the core building material in fields such as traffic engineering, marine engineering, and municipal infrastructure due to its excellent mechanical properties, economy, and durability. It is widely used in key structures like subway tunnels, sea-crossing bridges, sewage treatment plants, and converter stations [1–4]. However, in actual service environments, reinforced concrete structures often face the synergistic corrosion of multiple factors. Among them, the coupling effect of stray current and chloride salt is one of the main causes leading to premature deterioration and a significant reduction in the service life of structures. This situation not only threatens the safety of engineering structures but also incurs high maintenance and reinforcement costs, thereby triggering serious economic and social issues.

Stray current refers to the current that flows disorderly outside the designed circuit, with a wide range of sources and far-reaching impacts. In the field of urban rail transit,

when a subway system adopts DC traction power supply, part of the current will leak to the surrounding soil or groundwater through the steel rail, thus forming stray current that spreads along the line. In industrial scenarios, when equipment such as high-voltage converter stations and electrolysis workshops is in operation, if the grounding system is imperfect or the cable insulation is damaged, stray current will also be released into the surrounding environment [5–7]. Although the intensity of such current is usually in the milliampere range, it is persistent and mobile, which can change the electrochemical environment inside reinforced concrete. When the steel bar acts as the anode, its surface passivation film will undergo oxidative dissolution under the action of the current, with the reaction formula being $Fe - 2e^- = Fe^{2+}$. And Fe^{2+} will further react with OH^- and O_2 in the concrete pores to generate corrosion products such as $Fe(OH)_2$ and $Fe(OH)_3$. Since the volume of corrosion products is 2–6 times larger than that of the original metallic iron, tensile stress will be generated inside the concrete cover. When the stress exceeds the tensile strength of the concrete, cracking and spalling will occur in the cover, thus forming a vicious cycle of "corrosion–cracking–accelerated corrosion" [8–11].

Chloride salt is another key factor that exacerbates the corrosion of reinforced concrete. It is widely present in marine environments, saline soil areas, and regions where deicing agents are used in winter. The corrosion effect of chloride salt on steel bars is mainly achieved through the "depassivation" mechanism: Cl^- has extremely strong penetrability and can enter the interior of concrete through capillary adsorption, diffusion, and permeation in the concrete pores. When the Cl^- concentration on the surface of a steel bar reaches a critical threshold, it disrupts the integrity of the passivation film, thereby initiating the formation of a localized corrosion cell [12–15]. In practical engineering, stray current and chloride ions often interact, producing a synergistic effect far greater than the sum of individual factors [16]. For instance, Liu H et al. [17] found that stray current accelerates chloride ion migration, significantly shortening corrosion initiation time. Zhang Y et al. [18] further demonstrated that stray current increases ion mobility and reduces polarization resistance, intensifying steel corrosion. However, the combined influence of varying current densities and chloride concentration on concrete cover cracking, steel corrosion rate, and current efficiency remains insufficiently explored. This study addresses this gap by systematically investigating the coupled deterioration mechanisms using electromigration and impressed-current methods, aiming to quantify their effects and develop a predictive model for concrete durability. Furthermore, when the protective layer thickness ranges from 50 mm to 60 mm, there is a notable increase in the critical current density required for initial pitting corrosion [19].

It is worth noting that in actual engineering, stray current and chloride salt often do not act alone but exhibit a strong coupling effect. Their deteriorating effect on reinforced concrete is much greater than the simple superposition of the effects of a single factor [16]. On the one hand, stray current will significantly accelerate the transmission rate of Cl^- in concrete: under the action of an electric field, Cl^-, as an anion, will migrate directionally towards the anode. Its migration coefficient is 10–100 times higher than that under natural diffusion conditions. This allows the critical Cl^- concentration to be quickly reached on the surface of the steel bar, thereby significantly shortening the initiation time of corrosion [20]. Previous studies have highlighted that stray current significantly accelerates the deterioration of reinforced concrete by increasing the chloride ion migration rate and intensifying anodic dissolution. Under the influence of an electric field, chloride ions migrate rapidly toward the steel reinforcement, drastically shortening the corrosion initiation period. These findings reinforce the importance of studying the coupled effect of chloride ions and stray current, which can result in more severe deterioration than either factor acting alone. They found that a stone powder content of 3–8% makes the microstructure of concrete denser,

reduces the porosity, lowers the level of free chloride ions, increases the polarization resistance of corroded steel bars, decreases the corrosion current density, and reduces the mass loss of steel bars.

Although previous studies have extensively investigated the corrosion mechanisms of reinforced concrete under either chloride attack or stray direct current (DC) independently, the synergistic effects of both factors have not been systematically explored. In particular, the coupled influence of current density and chloride concentration on concrete cover cracking time, steel corrosion rate, and current efficiency remains unclear, and existing predictive models fail to capture the real deterioration behavior under combined exposure conditions. Therefore, this study aims to elucidate the coupled deterioration mechanism of chloride ions and stray DC through accelerated corrosion experiments employing both electromigration and impressed-current methods. Furthermore, it quantitatively analyzes their effects on steel corrosion and concrete cracking and establishes a predictive model for cracking time based on current density and chloride concentration, providing theoretical guidance for durability design of reinforced concrete structures in urban rail transit and coastal engineering environments. In recent years, extensive studies have examined the corrosion behavior of reinforced concrete (RC) under either chloride exposure or stray direct current (DC), providing a valuable foundation for understanding their respective deterioration mechanisms. However, most existing research has focused on single environmental factors, while the synergistic corrosion mechanisms under the combined influence of chloride ions and stray DC remain insufficiently explored. In particular, the interrelationship between steel corrosion rate, concrete cover cracking time, and current efficiency under varying current densities and chloride concentrations has not been clearly established. To address this gap, this study employs both electromigration and impressed-current acceleration methods to systematically investigate the coupled effects of chloride and stray DC, elucidate their influence on RC deterioration, and develop a quantitative predictive model. Therefore, conducting research on the deterioration of reinforced concrete under the coupled action of stray current and chloride salt not only holds significant theoretical value but also can provide a scientific basis for the protective design and lifespan prediction of engineering structures, meeting an urgent practical demand. The innovation of this study lies in systematically revealing the synergistic corrosion mechanism of reinforced concrete under the combined influence of chloride ions and stray direct current (DC), elucidating the coupled characteristics and mutual acceleration effects of the two environmental factors during the corrosion process. Through accelerated tests combining the electromigration and impressed-current methods, a quantitative predictive relationship between cracking time, current density, and chloride concentration has been established, leading to the development of a novel service-life prediction model that more accurately reflects the deterioration process under real exposure conditions. Moreover, this study identifies the deviation patterns between current efficiency and actual corrosion loss, providing a valuable reference for the interpretation and application of electrochemical acceleration results in practical durability design. The findings of this study not only deepen the scientific understanding of coupled corrosion mechanisms in reinforced concrete but also provide important engineering guidance for enhancing the durability, safety, and service life of structures exposed to complex electrochemical environments—such as metro systems, coastal regions, and electrified railways—thereby enriching the theoretical framework of reinforced concrete under multifactor coupled corrosion.

2. Materials and Testing

2.1. Materials

The raw materials used in this study consist of cement, silica fume, fly ash, fine aggregate, coarse aggregate, water, water-reducing agent, steel bars, metal electrodes, and chemical reagents. The specific performance indicators and sources of these materials are listed in Table 1. Huaxin-brand P·O 42.5 ordinary Portland cement was selected, with its chemical composition and mechanical properties also provided in Table 1.

Table 1. Test results for chemical composition and mechanical properties of cement.

Chemical Composition/%						Flexural Strength/MPa		Compressive Strength/MPa	
Sulfur trioxide	Magnesium oxide	Chloride ion	Alkali content	Free calcium oxide	Other components	3 d	28 d	3 d	28 d
2.68	3.82	0.054	0.62	0.78	92.046	5.4	8.0	31.3	46.8

The silica fume used in the tests is microsilica powder (Elkem Trading Co., Ltd, Oslo, Norway). The detailed chemical composition of the HPB300 steel is provided in Appendix A. The data were obtained from the manufacturer's specifications and the Chinese standard GB/T 1499.1-2008; Steel for the reinforcement of concrete—Part 1: Hot rolled plain bars. Beijing, China, 2008 [21]. Its performance indicators meet the requirements specified in GB/T 27690-2023 [22]. The main physical performance indicators are provided in Table 2, while the chemical composition is detailed in Table 3.

Table 2. Physical properties of silica fume.

Specific Surface Area/ (m^2/kg)	Density/(kg/m^3)	Alkali Content/%	Water Demand Ratio/%	Loss on Ignition/%
22,453	2220	0.18	112	1.48

Table 3. Chemical composition of silica fume (%).

SiO_2	CaO	SO_3	K2O	P_2O_5	Fe_2O_3	GeO_2	TiO_2	MnO	CuO	ZnO
98.22	0.63	0.44	0.40	0.22	0.05	0.04	0.01	0.01	0.01	0.01

The fly ash used in this study is Grade I, with performance indicators that comply with the specifications outlined in GB/T 1596-2017 [23]. The fine aggregate is natural river sand, which has an apparent density of 2622 kg/m^3. Its measured mud content is 3.1%, moisture content is 0.7%, and the particle size range is 0–5 mm. A sieve analysis revealed a fineness modulus of 3.0, classifying the sand as medium sand in Zone II. The coarse aggregate consists of crushed limestone, with an apparent density of 2715.79 kg/m^3 and a particle size range of 5–20 mm. The moisture content of the crushed stone is 0.4%, and the crushing index is provided in Table 4.

Table 4. Crushing value of crushed stone.

Group	Sample Quality/g	Residual Mass/g	Crushing Index/%	Average/%
Group One	3000	2793	6.9	8.3
Group Two	3000	2722	9.3	
Group Three	3000	2743	8.6	

The water-reducing agent used in this study is SY-PA, a polycarboxylate-based high-performance water-reducing agent, which appears as a light yellow liquid. The performance test results for this water-reducing agent are provided in Table 5. The steel bars employed were HPB300-grade with a diameter of 14 mm. Tensile tests were conducted on the steel bars following the guidelines of GB/T 228.1-2021 [24], and the results are presented in Table 6.

Table 5. Water-reducing agent test results.

Test Items	Standard Requirements	Test Results	Inspection Conclusion
Density/(g/cm^3)	1.04 ± 0.02	1.056	Qualified
pH	3~7	4.95	Qualified
Sodium sulfate content/%	≤5.0	0.74	Qualified
Chloride content/%	≤0.6	0.01	Qualified
Total alkali content/%	≤10.0	0.63	Qualified
Water reduction rate/%	≥25	35	Qualified
Gas content/%	≤6.0	3	Qualified
Water-loss ratio/%	≤60	21	Qualified

Table 6. Mechanical properties of reinforcing bars.

Reinforcing Bar Specifications	Yield Strength/MPa	Ultimate Strength/MPa	Modulus of Elasticity/GPa
Φ14 HPB300	387.53	537.19	200

The water-to-binder ratio of the concrete used in this test was set at 0.38, and the concrete mix proportions are listed in Table 7. The design parameters for the test are shown in Table 8. Additionally, a control group denoted as D0 was added to the experimental design to investigate the effect of chloride ions without the influence of stray current. The D0 series specimens were not electrified (0 mA/cm^2) and were exposed to slightly, moderately, and highly corrosive environments, respectively. This group serves as a reference for evaluating the impact of current density on corrosion and cracking behavior. In this table, the specimen numbering format is D/M x-y, where "D/M" represents electromigration/powered corrosion testing, "x" denotes the current density, and "y" corresponds to the chloride salt environment. Specifically, "W", "Z", and "Q" indicate slight, moderate, and severe corrosion environments, respectively.

Table 7. Concrete mix proportions.

Strength Grade (MPa)	Cement (kg/m^3)	Fly Ash (kg/m^3)	Silica Fume (kg/m^3)	Coarse Aggregate (kg/m^3)	Fine Aggregate (kg/m^3)	Water (kg/m^3)	Water-Reducing Agent (%)
C40	285	120	25	1167	629	165	17.2

Table 8. Experimental parameter design.

Specimen Number	Test Method	Power Supply Method	Chloride Environment	Number of Test Specimens
D0.5-W	Electromigration	0.5 mA/cm^2, continuous current	Slightly corrosive	2
D0.5-W			Slightly corrosive	2
D0.5-Z			Moderately corrosive	2
D0.5-Q			Highly corrosive	2
D3.0-W		3 mA/cm^2, energized for 4 h, de-energized for 20 h	Slightly corrosive	2
D3.0-Z			Moderately corrosive	2
D3.0-Q			Highly corrosive	2
M0.5-W	Electrical corrosion	0.5 mA/cm^2, continuous current	Slightly corrosive	2
M0.5-Z			Moderately corrosive	2
M0.5-Q			Highly corrosive	2
M3.0-W		3 mA/cm^2, energized for 4 h, de-energized for 20 h	Slightly corrosive	2
M3.0-Z			Moderately corrosive	2
M3.0-Q			Highly corrosive	2

2.2. Testing

2.2.1. Specimen Preparation

This study designed two types of specimens based on the test requirements: one for the electromigration test and the other for the powered corrosion test. The fabrication process is illustrated in Figure 1. For the electromigration test, the specimen is a concrete cube measuring 100 mm × 100 mm × 100 mm, with an embedded HPB300-grade steel bar. The steel bar has a diameter of 14 mm and a length of 120 mm, positioned at the center of the cube, surrounded by a protective layer of 43 mm thickness. The specimen for the powered corrosion test is a concrete cylinder with a diameter of 100 mm and a length of 180 mm. It contains an HPB300-grade steel bar, also with a diameter of 14 mm and a length of 200 mm. The steel bar is centrally located within the cylinder, with anti-corrosion treatment applied to the ends (50 mm at each end). The protective layer around the bar is 43 mm thick.

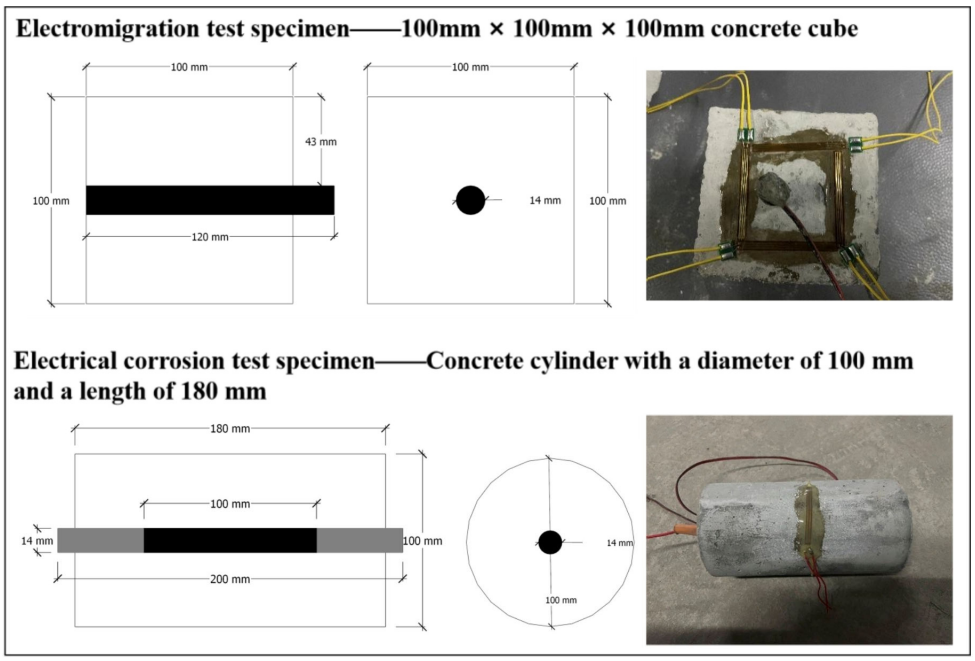

Figure 1. Specimen dimensions.

As shown in Figure 2, before the test, the steel bars need to be cut to a fixed length and have their ends ground flat. Subsequently, in accordance with the standard GB/T50082-2024 [25], the following operations were carried out in sequence: pickling with 12% hydrochloric acid, neutralization in a double-tank $Ca(OH)_2$ solution, rinsing with clean water, and drying at 108.5 °C for 60 min. After completing these operations, the initial mass of the steel bar was weighed (accurate to 0.001 g), and it was checked to ensure there is no rust. Then, a 1 mm^2 copper wire was tied to one end of the steel bar, and it was sealed using insulating tape + waterproof adhesive. After that, a 120-3AA strain gauge was attached to the middle section of the steel bar, and a thin layer of waterproof adhesive was applied to prevent water ingress. Positioning fixtures are placed on both ends of the steel bar. For the specimens subjected to powered corrosion, insulation treatment was also required at 50 mm from each end of the steel bar, resulting in an exposed length of 100 mm and an area of 43.98 cm^2. Subsequently, the concrete was mixed, with the mixing time controlled to be $\leq$ 210 s and a slump of 140 mm. The concrete was formed by tamping and vibrating in two layers, and the surface was covered with plastic wrap. After the specimens were left to stand for 36 h in a standard curing room at 20 °C and RH > 50%, the molds were removed, and the specimens were numbered. Then, they were transferred to a curing chamber at

20 °C and RH 96% for 28 d of curing. After measurement, the 28 d compressive strength was 41.4 MPa, and the tensile strength was 3.94 MPa. After the curing was completed, simulated corrosive soil with a water content of 15% was prepared. It was specifically divided into a slight corrosion group (Cl^- 50 mg/kg, using natural river sand), a moderate corrosion group (Cl^- 1350 mg/kg, using original soil from Hami, Xinjiang), and a severe corrosion group (Cl^- 5500 mg/kg, by adding NaCl solution to the original soil, mixing, and drying). After drying and adding water, it was set aside for subsequent powered corrosion and electromigration tests.

Figure 2. Reinforcement processing and specimen forming.

2.2.2. Corrosive Environment

In this experiment, the corrosive medium for the powered corrosion test and the cathode conductor in the electromigration test are both corrosive soils prepared in the laboratory. As shown in Table 9, three groups are established: slight corrosion, moderate corrosion, and severe corrosion. Among them, the slight corrosion control group uses natural river sand from a certain location in Anhui, with a Cl^- content of 50 mg/kg. The moderate corrosion group directly utilizes the surface soil from the Beihuan Converter Station in Hami, Xinjiang, and the measured Cl^- content of this soil sample is 1350 mg/kg. For the severe corrosion group, a high-concentration NaCl solution was added to the moderate corrosion soil, mixed thoroughly, and dried, increasing the Cl^- content to 5500 mg/kg. As shown in Figure 3, the water content of the corrosive soils prepared in this experiment is uniformly set at 15%. The temporal variation in concrete resistivity reflects the evolution of pore-solution conductivity and corrosion activity. As chloride concentration increases, ion mobility within the concrete matrix rises, resulting in a marked decrease in resistivity. At higher current densities, intensified electrochemical reactions further reduce resistivity due to enhanced electron pathways. This indicates that chloride ingress and stray current jointly enhance the electrical conductivity of concrete, thereby accelerating the corrosion process and demonstrating a clear synergistic effect.

Table 9. Soil corrosivity rating.

Corrosion Rating	Weak	Medium	Strong
Chloride content in soil/(mg/kg)	250~500	500~5000	>5000

(**a**)

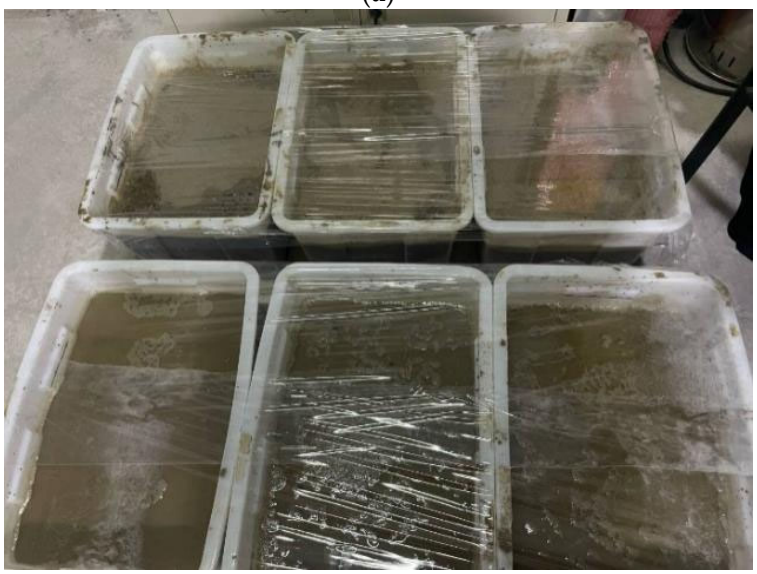

(**b**)

Figure 3. Configuration of simulated soil. (**a**) Preparation process of corrosive soils with different chloride contents; (**b**) Experimental setup for soil resistivity measurement.

2.2.3. Electrical Corrosion Test

The powered accelerated corrosion method was employed to conduct the corrosion test. During this process, the steel bar acts as the anode, undergoing an oxidation reaction, while the external cathode experiences a reduction reaction. The design and fabrication process are shown in Figure 4. After 28 days of standard curing, the reinforced concrete specimens were coated with insulating epoxy resin at both ends. A strain gauge was attached to the middle of the cathode side, and the entire specimen was sealed with waterproof adhesive to prevent water ingress. To reduce resistance, the specimens were first soaked in a 3% NaCl solution for 3 days. Subsequently, they were vertically buried in corrosive soil with a burial depth of $\geq$ 140 mm. A cathode was placed 200 mm away

from the specimens, and they were powered for 20 days under a constant temperature of 25 °C. During the power-on period, water was added every 2 days to restore the initial mass, thereby stabilizing the water content. After the test, the specimens were split open to observe the deterioration of the concrete and the corrosion of the steel bars.

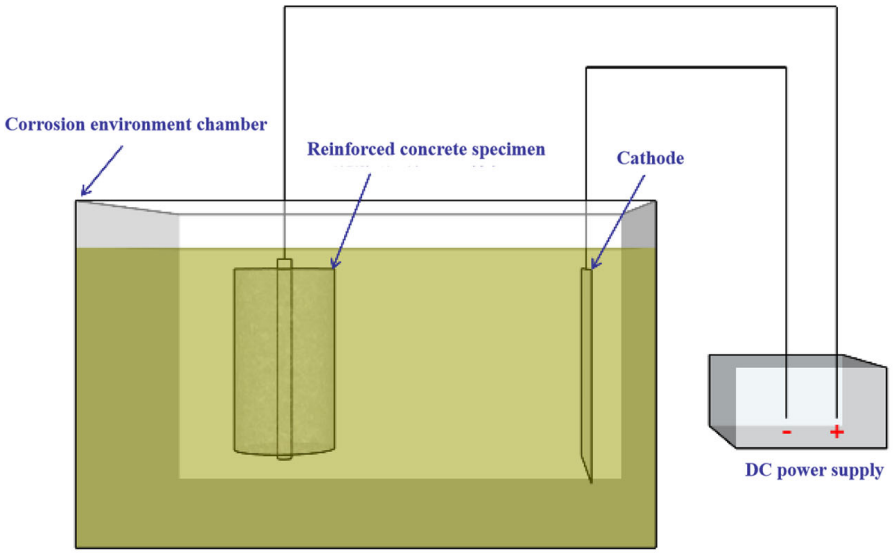

Figure 4. Electrically corroded test apparatus.

2.2.4. Electromigration Corrosion Test

The electromigration corrosion test apparatus used in this test is shown in Figure 5. The increasing trend of steel mass loss demonstrates that chloride exposure predominantly governs the corrosion process, while applied current density determines the corrosion rate. When the current density increases from 0.5 to 3.0 mA/cm^2, the mass loss accelerates significantly, corresponding to an enhanced anodic dissolution rate. It was also observed that higher chloride concentrations lead to looser and more porous corrosion products, which facilitate deeper electrolyte penetration and form an "acceleration loop." This indicates that chlorides not only enhance ionic conductivity but also disrupt the passive film, greatly amplifying the corrosion effect of stray current. During the test, the area on the surface of the steel bar where the current flows in serves as the cathode, and no corrosion occurs in this region. In contrast, the area where the current flows out is the anode. Under the combined influence of multiple factors such as current density, pH value, and chloride ion concentration, the surface of the steel bar at the anode undergoes corrosion, and its corrosion mechanism is consistent with that of stray current corrosion. After 28 days of standard curing, an open acrylic box was affixed to each side of the specimen, and waterproof sealing was carried out around the edges. Inside the boxes, corrosive soil was filled on the cathode side, and a 0.3 mol/L NaOH solution was injected on the anode side. A strain gauge was attached to the cathode end on the upper surface of the specimen. The entire setup was then soaked in a 3% NaCl solution for 3 days to reduce resistance. A 304 stainless steel electrode measuring 80 mm × 80 mm was used, and the test was powered for 20 days under a constant temperature of 25 °C. During the power-on period, the anode solution was replaced every 3 days, and the resistance of both electrodes was measured. The electrodes were replaced if necessary. The sealing around the edges of the boxes was checked daily, and the solution was replenished to the upper surface of the concrete. After the test, the specimens were split open to inspect the deterioration of the concrete and the corrosion of the steel bars.

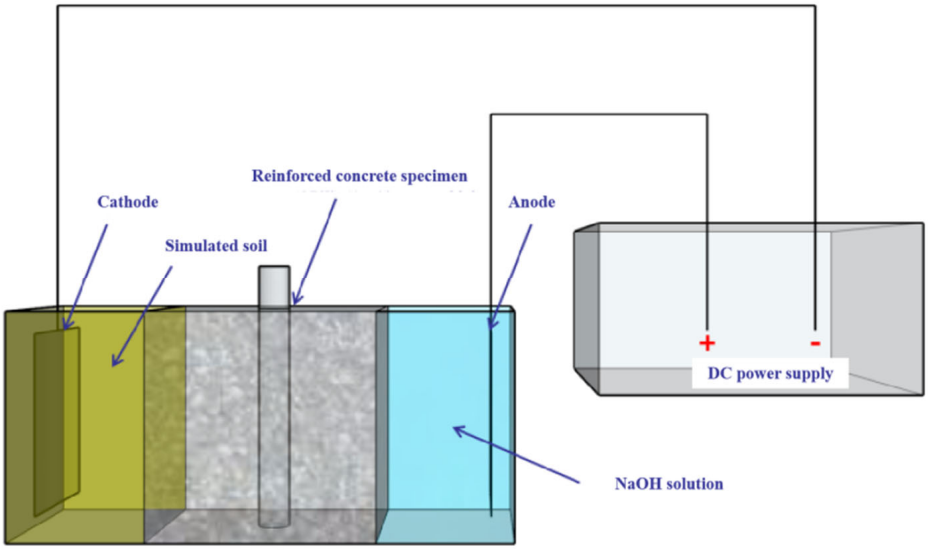

Figure 5. Electromigration corrosion test apparatus.

2.2.5. Soil Resistivity

Before measuring the soil resistivity, it was necessary to first insert four stainless steel electrodes into the soil at equal intervals and equal depths. In this test, the spacing between the metal electrodes was set at 150 mm, and the depth of electrode insertion into the soil was 1/20 of the electrode spacing. Thus, the depth of metal electrode insertion into the soil is 8 mm. The positive and negative terminals of a DC power supply were connected to metal electrode A and metal electrode B at the two ends, respectively. Metal electrodes C and D were connected to a voltmeter with a resolution of 1 mV to measure the voltage between electrodes C and D. The DC power supply was turned on to continuously supply power in a constant-current mode. After the voltage stabilized, the voltage VCD between electrodes C and D was recorded. Then, the measured soil resistivity ρ was calculated using Equation (1). Three different proportions of soil were used in this test. Each proportion of soil was evenly distributed into two environmental chambers. Three sets of points were selected for testing in each environmental chamber, and the average values were taken. The test results are shown in Table 10.

$$\rho = 2\pi L \frac{V_{CD}}{I_{AB}} \quad (1)$$

where

P represents the soil resistivity, with the unit of Ω·m;
L denotes the electrode spacing, with the unit of m;
V_{CD} is the potential difference between electrodes C and D, with the unit of V;
I_{AB} refers to the current between electrodes A and B, with the unit of A.

Table 10. Soil resistivity test values in each environmental chamber.

Chloride Environment	Number	VCD/V	IAB/A	ρ/(Ω·m)
Slightly corrosive	1	40.26	0.1	309.504
	2	41.07	0.1	303.399
Moderately corrosive	1	19.92	0.1	145.972
	2	19.37	0.1	150.117
Highly corrosive	1	12.39	0.1	93.371
	2	12.65	0.1	95.330

2.2.6. Chloride Content

Three-point sampling was carried out in the corrosive soil prepared in the laboratory. Subsequently, the soil samples were placed in an oven at 108 °C and dried for 6 h. After being taken out, they were allowed to cool to room temperature in a dry environment. Then, 50 g of soil samples were weighed and put into a container, and 450 milliliters of deionized water were poured in. After fully stirring the soil solution, a DY-2501B chloride ion content tester was used to measure the chloride ion concentration in the soil solution. The test results are presented in Table 11.

Table 11. Chloride ion content in corrosive soils.

Chloride Environment	Number	Actual Measured Values of Chloride Ion Content in Soil/(mg/kg)
Slightly corrosive	1	48.7
	2	53.6
Moderately corrosive	1	1336.8
	2	1344.2
Highly corrosive	1	5401.5
	2	5429.6

2.2.7. Reinforcing Steel Corrosion Rate

The difference in the mass of the steel bar before and after corrosion, minus the correction value, is the actual measured corrosion amount of the steel bar. Since the ends of the steel bar in this paper are insulated and do not participate in the corrosion reaction, the actual measured corrosion rate of the steel bar is calculated according to Equation (2). The theoretical corrosion amount of the steel bar is obtained using Faraday's law of electrolysis, as shown in Equation (3).

$$\chi = \frac{L_1(M_0 - M_1)}{L_0 M_0} \times 100\% \quad (2)$$

where

χ represents the actual measured corrosion rate of the steel bar, with the unit of %;

M_0 denotes the initial mass of the entire steel bar, with the unit of g;

M_1 refers to the mass of the entire steel bar after corrosion, with the unit of g;

L_0 is the length of the steel bar participating in the corrosion, taken as 100 mm;

L_1 represents the total length of the entire steel bar. For the powered corrosion specimen, it is taken as 200 mm, and for the electromigration specimen, it is taken as 120 mm.

$$m_F = \frac{MIt}{nF} \quad (3)$$

where

mF represents the theoretical mass of metal dissolved, with the unit of g;

M denotes the molar mass of the metal, with the unit of g/mol;

I refers to the current intensity, with the unit of A;

t is the power-on time, with the unit of s;

n represents the ionic charge number, which is dimensionless and taken as 2;

F is Faraday's constant, taken as 96,485 C/mol.

3. Results and Discussion

3.1. Differences in Concrete Deterioration Under Various Testing Methods

Figure 6 illustrates the changes in concrete resistivity over time under different powering methods. During the soaking stage, the initial resistivity of the specimens is ap-

proximately 142 Ω·m, which decreases to 87 Ω·m after 3 days of soaking. The decline in resistivity during this stage is closely related to changes in the internal pore structure of the concrete and water penetration. The impact of initial soaking on resistivity is significant. In the powered corrosion test, the resistivity drops rapidly with the powering time in the early stage and stabilizes at around 50 Ω·m in the short term. This is because insufficient soaking in the early stage results in unsaturated concrete. After powering on, the concrete continuously absorbs water, and the inward diffusion of chloride ions significantly enhances its conductivity [26]. In the later stage of the test (3–5 days before cracking), the resistivity experiences a slight increase, which is attributed to the intensified deterioration of the concrete, causing local dissolution of the matrix. The increased porosity leads to a reduction in conductivity [27]. At the initial stage of the electromigration test, the resistivity shows a trend of "rising first and then falling", which stems from the fact that the specimens are in contact with the solution only on two sides. The evaporation of electrolyzed water on the surface and the uneven distribution of water at the anode and cathode under the electric field result in temporary drying [28]. Subsequently, the resistivity enters a continuous declining stage, and the rate of decline gradually slows down and stabilizes over time.

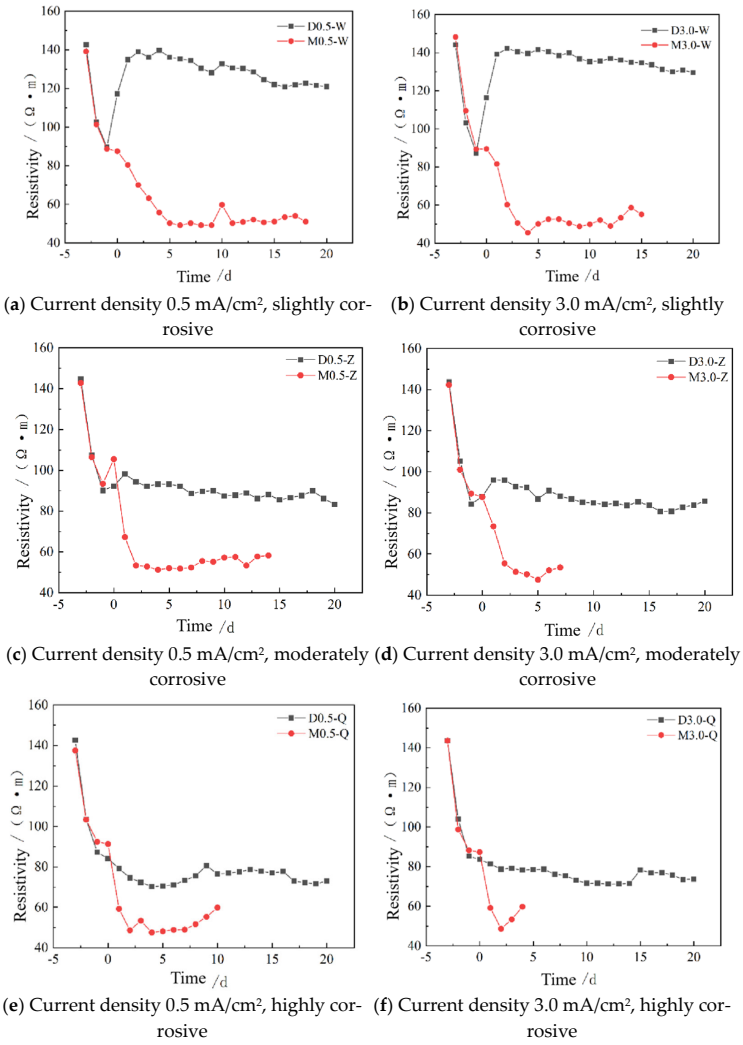

(**a**) Current density 0.5 mA/cm², slightly corrosive

(**b**) Current density 3.0 mA/cm², slightly corrosive

(**c**) Current density 0.5 mA/cm², moderately corrosive

(**d**) Current density 3.0 mA/cm², moderately corrosive

(**e**) Current density 0.5 mA/cm², highly corrosive

(**f**) Current density 3.0 mA/cm², highly corrosive

Figure 6. Time-dependent variation in concrete resistivity under different energization methods. Note: Concrete resistivity measurements begin at −3 days; −3 indicates the specimen prior to immersion, 0 indicates the specimen after three days of immersion and prior to test preparation, 1 indicates the first day of testing, and so on. Since the total circuit resistance cannot be used to calculate concrete resistivity after the electrically induced corrosion specimen cracks, resistivity is only calculated up to the day before cracking occurs.

The cracking times of the concrete cover under different working conditions are shown in Figure 7. It can be observed from the figure that both the chloride salt concentration and current density are crucial factors affecting the cracking of the concrete cover, and the deterioration patterns are similar under the two test methods. However, under the same conditions, the cracking times of the specimens subjected to electromigration corrosion are all later than those of the specimens subjected to powered corrosion. This indicates that the electromigration method causes relatively slower damage to the concrete cover. In addition, the crack width of the specimens subjected to electromigration corrosion is mainly influenced by the chloride salt concentration, while the crack width of the specimens subjected to powered corrosion primarily depends on the presence or absence of chloride salts.

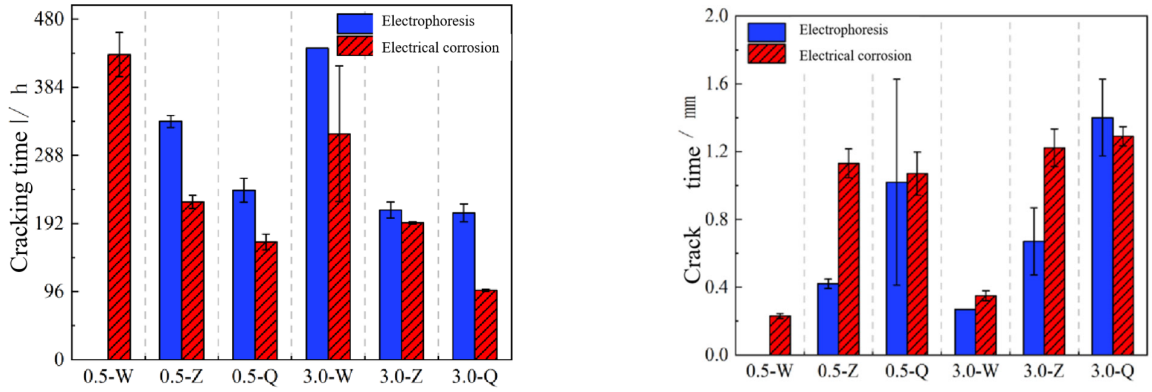

(**a**) Concrete Cracking Time (**b**) Maximum Crack Width on Day 20

Figure 7. Cracking of concrete cover layers in test specimens under different testing methods.

In this paper, the $AgNO_3$ colorimetric method proposed by Otsuki et al. [29] is employed to determine the extent of chloride ion erosion. A 0.1 mol/L $AgNO_3$ solution is sprayed onto the concrete surface. Where Cl^- is present, white AgCl is formed, while in areas without Cl^-, AgOH rapidly transforms into brownish Ag_2O, creating a distinct boundary. After the colors stabilize, the white region indicates the eroded area. Following a 20-day stray current corrosion test, the electromigration specimens are subjected to Cl^- erosion on only one side. Therefore, a 100 t electro-hydraulic servo universal testing machine is used to vertically split the specimens along the eroded surface, and then the $AgNO_3$ solution is directly sprayed onto the fresh split surface. For the powered corrosion specimens, a cutting machine is used to split them in the center along the direction perpendicular to the steel bar, and the colorimetric operation is carried out on the cross-section. The results of chloride ion erosion are shown in Figures 8 and 9. The microscopic observations further confirm the macroscopic corrosion trends. In the electromigration specimens, corrosion pits were scattered and mainly located along microcracks on the steel surface, while the impressed-current specimens exhibited distinct strip-shaped pitting with much greater depth. This indicates stronger electrochemical activity under impressed-current conditions, where localized anodic dissolution dominates, leading to accelerated failure of reinforcement. These observations are consistent with the macroscopic mass loss and cracking time trends, validating the proposed interpretation of the coupled corrosion mechanisms. As shown in Figures 8–10, the deterioration behavior of concrete and the corrosion morphology of steel reinforcement varied significantly between the electromigration and impressed-current methods. The electromigration specimens exhibited delayed cracking but deeper chloride penetration, while the impressed-current specimens showed faster cracking and more localized corrosion pits. This difference can be attributed to the distinct ion transport and electrochemical reaction mechanisms of the two test setups. The findings demonstrate

that the selection of test method has a substantial influence on both the corrosion rate and failure mode, which should be considered when evaluating the durability of reinforced concrete under coupled chloride–current environments.

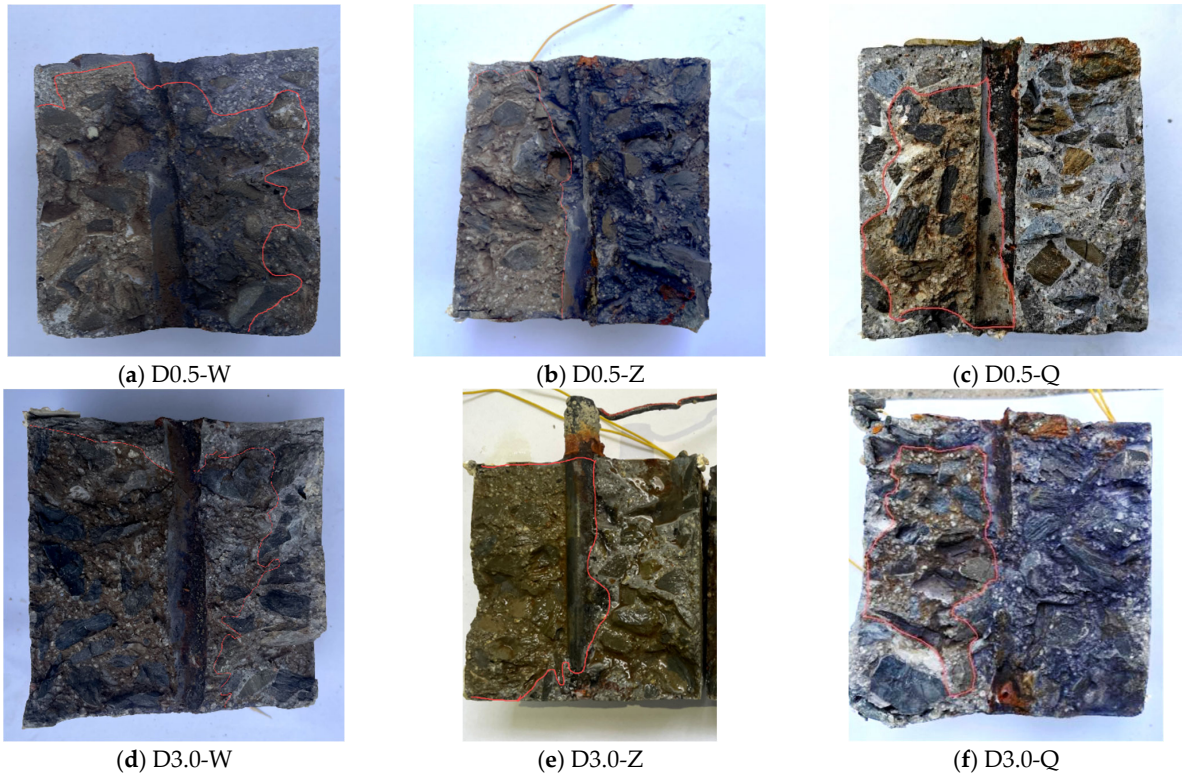

(**a**) D0.5-W (**b**) D0.5-Z (**c**) D0.5-Q

(**d**) D3.0-W (**e**) D3.0-Z (**f**) D3.0-Q

Figure 8. Chloride ion corrosion zones of electromigration test specimens.

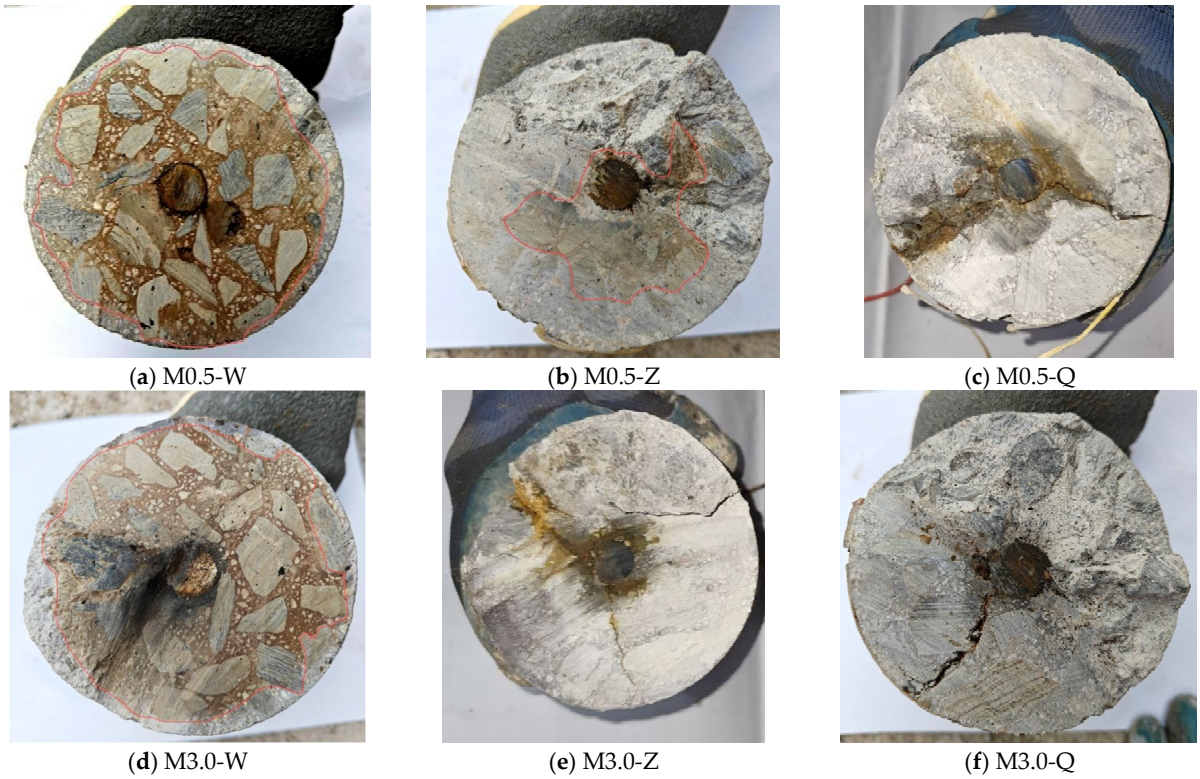

(**a**) M0.5-W (**b**) M0.5-Z (**c**) M0.5-Q

(**d**) M3.0-W (**e**) M3.0-Z (**f**) M3.0-Q

Figure 9. Chloride ion corrosion zone on electrically corroded specimen.

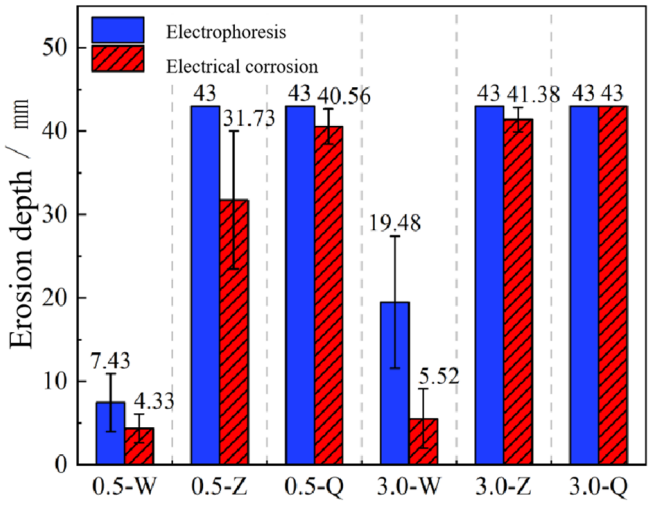

Figure 10. Chloride ion corrosion depth. Note: 43 mm, a corrosion depth of 43 mm indicates that chloride ions have reached the reinforcement surface.

As shown in Figure 9, the red-colored regions represent high chloride ion concentrations detected by $AgNO_3$ colorimetric reaction, while lighter areas correspond to lower chloride contents. The distinct red zones in specimens subjected to higher current densities indicate deeper chloride penetration and more pronounced corrosion initiation. The boundary between red and non-colored regions marks the chloride erosion front, which was used to quantify the penetration depth. The coupled effect of chloride ions and stray current significantly accelerates both the electrochemical corrosion of reinforcement and the physical degradation of concrete. As the current density increases, the electric field enhances chloride ion migration toward the steel surface, leading to faster depassivation and localized corrosion. Simultaneously, the accumulation of corrosion products generates expansive stresses, resulting in microcracks and loss of stiffness in the surrounding concrete matrix. These combined electrochemical–mechanical interactions explain the observed rapid deterioration in both corrosion rate and cracking behavior compared with the single chloride or current conditions. The measurement was carried out using the ruler-and-compass method. A vernier caliper and a straightedge were employed to measure the discoloration depth of chloride ions after wet–dry cycles. A discoloration depth value was read every 10 mm, and the average of seven discoloration depth values was taken as the chloride ion erosion depth. The measurement results are presented in Figure 10. As shown in the figure, the chloride ion erosion depth in the electromigration specimens is notably greater than in the powered corrosion specimens under the same conditions. With the increase in current density, the corrosion morphology of steel bars changes significantly, as shown in Figure 10. The amount of corrosion also rises, leading to more pronounced corrosion pits and surface roughening. In particular, specimens D5.0-Q (highly corrosive environment with 5.0 mA/cm^2) exhibit deep, strip-shaped corrosion pits, while D0.5-Z (moderately corrosive environment with 0.5 mA/cm^2) show shallow and uniformly distributed pits. These observations confirm that higher current density intensifies localized corrosion and accelerates damage propagation on the steel surface. This suggests that, during the electromigration test, chloride ions migrate toward the steel bar surface under the influence of the applied electric field, leading to a faster erosion rate. In contrast, in the powered corrosion test, chloride ions migrate from the entire concrete surface. The chloride ion erosion area of the electromigration specimens is mainly concentrated on the side of the specimen near the negative electrode, while the chloride ion erosion area of the powered corrosion specimens is relatively uniform and mainly concentrated near the

concrete surface [30–32]. Both show a significant trend of increasing depth and extent of the erosion area with an increase in chloride salt concentration.

3.2. Differences in Reinforcing Bar Corrosion Under Various Test Methods

The theoretical corrosion amount, actual measured corrosion amount, and the actual measured corrosion rate of steel bars in concrete under all working conditions were calculated. The comparison between the theoretical corrosion amount (calculated based on Faraday's first law of electrolysis) and the actual corrosion amount is shown in Figure 11.

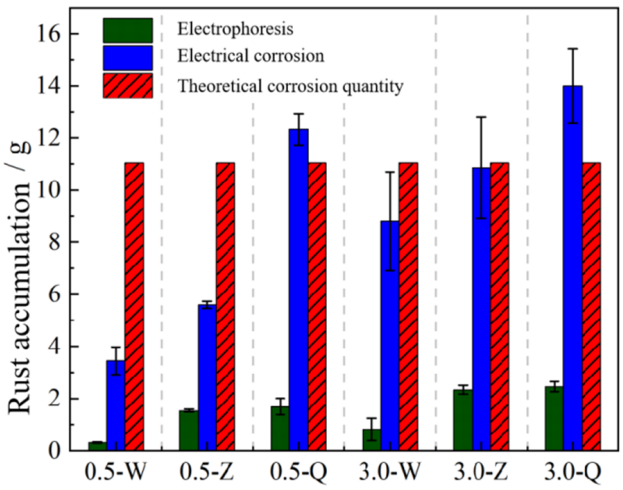

Figure 11. Comparison of reinforcing bar corrosion quantity under different test methods and theoretical corrosion quantity.

Under the same conditions, the corrosion amount in the electromigration specimens is significantly smaller than in the powered corrosion specimens. Additionally, both chloride salt concentration and current density have a substantial impact on the steel bar corrosion rate. As chloride salt concentration increases, the actual measured corrosion rate of the steel bar also increases; similarly, a higher current density results in a higher corrosion rate.

There is a notable difference between the theoretical corrosion amount, as calculated by Faraday's law of electrolysis, and the actual measured corrosion amount. This suggests that the theoretical corrosion amount is an idealized value, determined by parameters such as current intensity, power-on time, and the metal's molar mass. In contrast, the actual corrosion amount is influenced by various factors, including the thickness of the concrete cover, chloride ion concentration, current density, and the test methods used.

The morphology of the electromigration specimens after corrosion is shown in Figure 12, while the corrosion morphology of the powered corrosion specimens is displayed in Figure 13. The corrosion characteristics of the steel bars are significantly influenced by both current density and chloride ion concentration. For the electromigration specimens, as the chloride ion concentration increases, the amount of steel bar corrosion also rises, leading to more pronounced corrosion pits. When the current density increases, the corrosion sites show a relatively rough pitting morphology, with noticeable signs of intergranular corrosion.

In the case of the powered corrosion specimens, an increase in chloride ion concentration results in a significant acceleration of the corrosion rate, leading to the formation of large striped corrosion pits on the steel bars. This is linked to the cracking of the concrete cover. As current density increases, local corrosion intensifies, forming distinct corrosion pits. These effects are consistent with findings from previous studies [33].

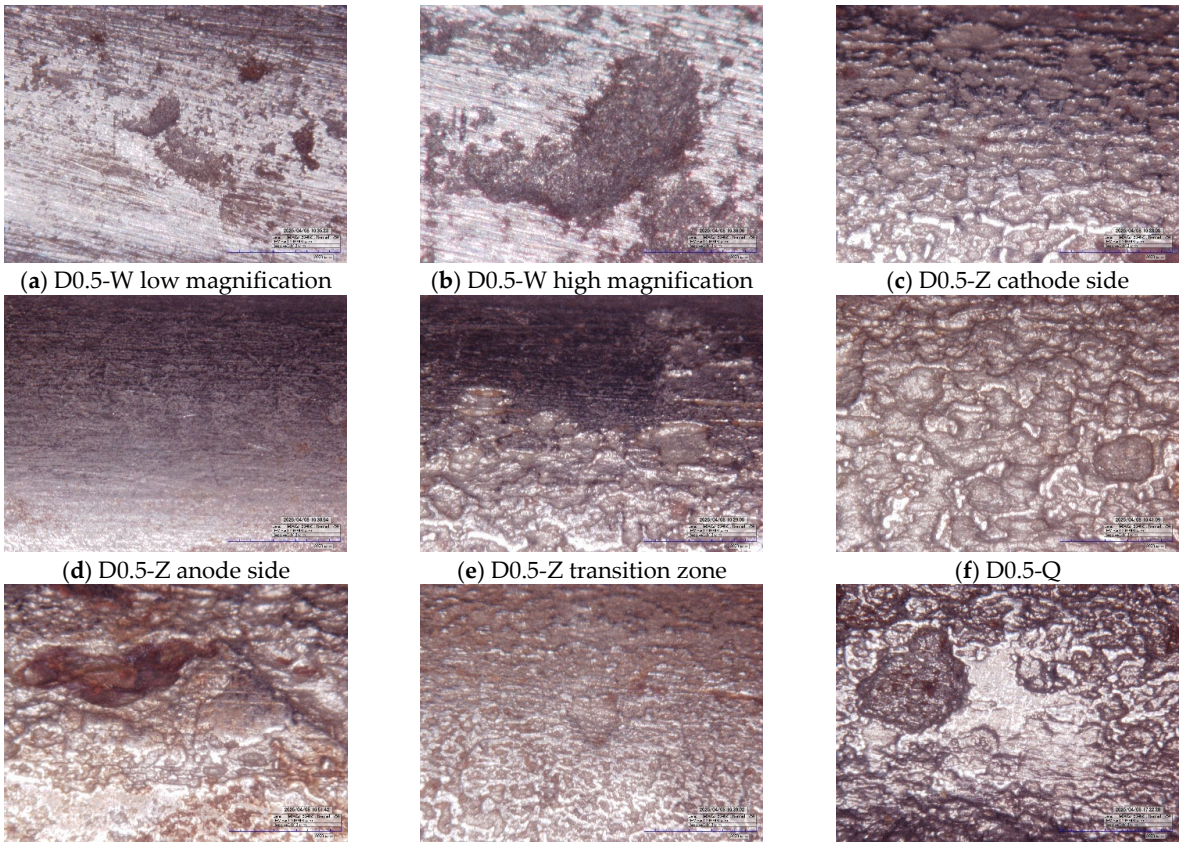

(**a**) D0.5-W low magnification (**b**) D0.5-W high magnification (**c**) D0.5-Z cathode side

(**d**) D0.5-Z anode side (**e**) D0.5-Z transition zone (**f**) D0.5-Q

(**g**) D3.0-W (**h**) D3.0-Z (**i**) D3.0-Q

Figure 12. Corrosion morphology of reinforcing bars in electromigration test specimens.

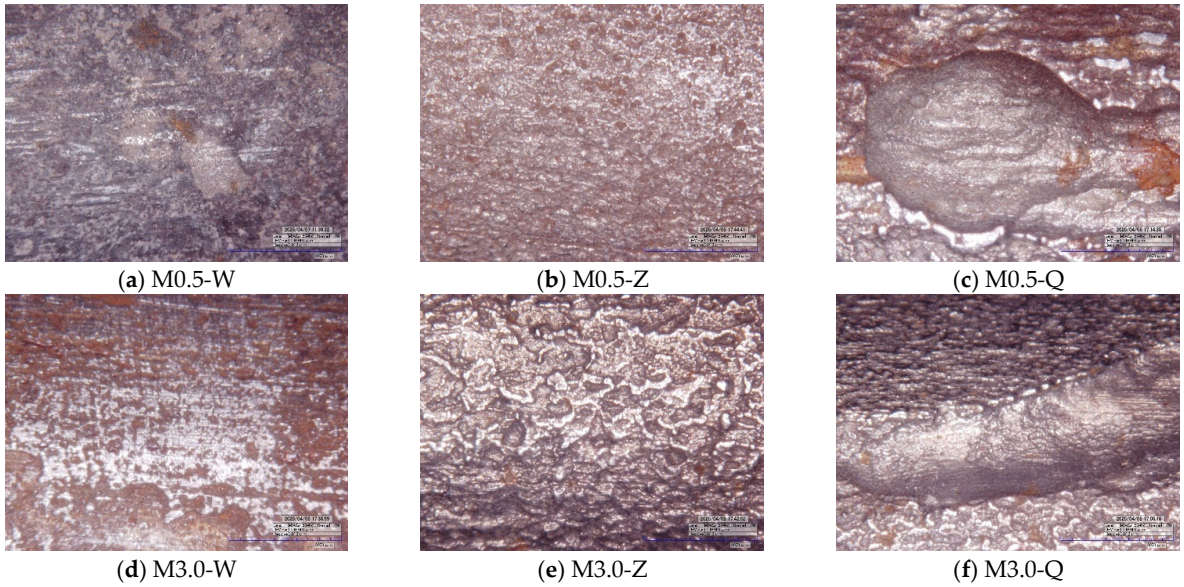

(**a**) M0.5-W (**b**) M0.5-Z (**c**) M0.5-Q

(**d**) M3.0-W (**e**) M3.0-Z (**f**) M3.0-Q

Figure 13. Corrosion morphology of steel bars in electrically powered corrosion test specimens.

3.3. Analysis of Performance Degradation in Concrete Under Coupling Effects

Periodic powering of specimens can lead to a significant increase in the internal temperature of the concrete, which, in turn, promotes the migration of water and chloride ions. This situation may have a certain impact on the concrete resistivity. Therefore, in this experiment, the concrete resistance was measured before the start of each powering cycle. The variation patterns of the concrete resistivity of each specimen over time under different environmental factors are shown in Figure 14. Except for the highly corrosive

environment, the concrete resistivity of the specimens in the other groups shows varying degrees of increase in the early stage of the experiment. This phenomenon can be attributed to the fact that the side surfaces of the electromigration specimens are exposed to the air, and the surface water evaporates, leading to an increase in the concrete resistivity [34]. For the control group without stray current interference, the concrete is only affected by the chloride salt environment. In this case, ions mainly enter the concrete through diffusion, causing the concrete resistivity to decrease uniformly and slowly over time. This indicates that when there is no stray current, the diffusion of chloride ions is the main factor affecting the change in concrete resistivity [27].

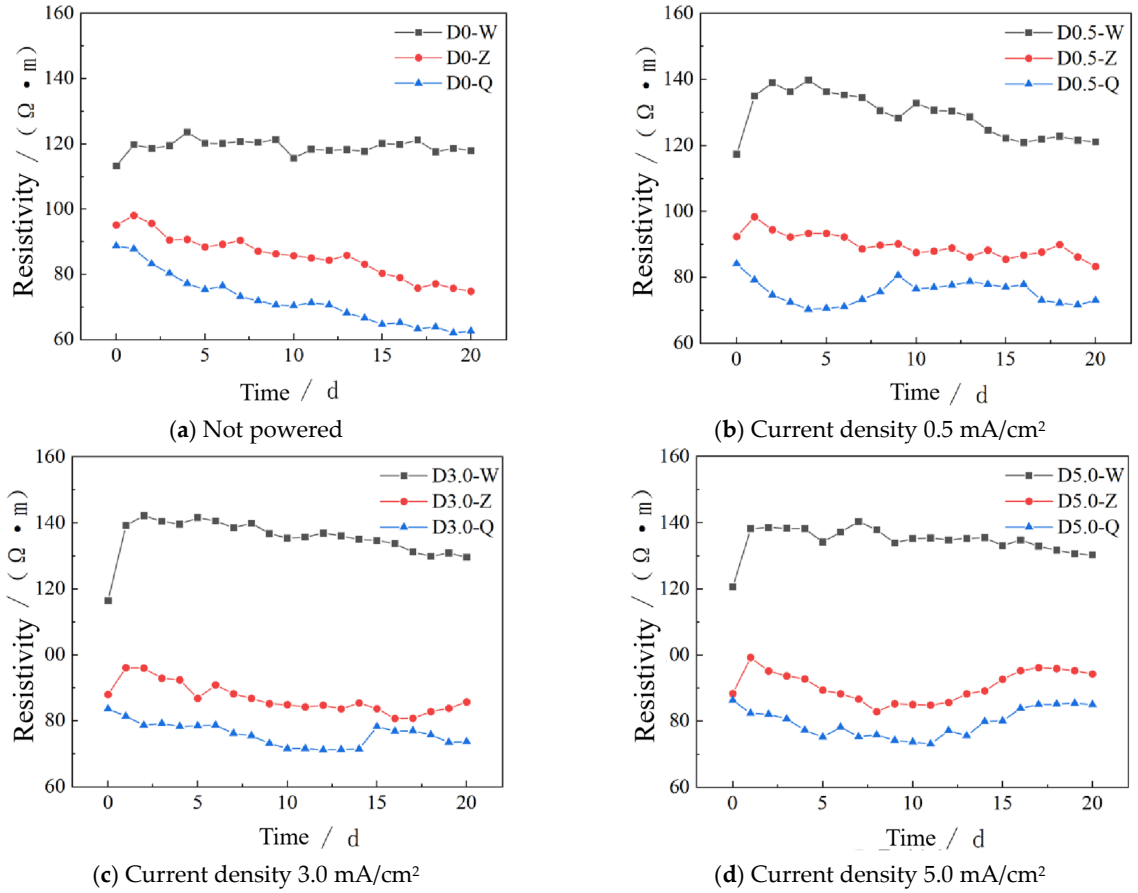

(**a**) Not powered (**b**) Current density 0.5 mA/cm²

(**c**) Current density 3.0 mA/cm² (**d**) Current density 5.0 mA/cm²

Figure 14. Time-dependent variation in concrete resistivity under different environmental factors.

Under the interference of stray currents, since the average current is the same for each group of specimens, the variation patterns of the concrete resistivity in the early stage are similar under different current densities. This indicates that in electromigration specimens, the main factor affecting the degree of chloride ion diffusion under the same chloride ion concentration is the total electric flux rather than the maximum current density. However, in the later stage of powering, as the concrete matrix deteriorates, the resistivity will gradually increase, and this phenomenon will occur earlier with an increase in current density.

In various chloride salt environments, an increase in chloride ion concentration results in a decrease in the concrete's resistivity. This is because after chloride ions penetrate into the concrete through diffusion and the driving effect of the current, they can reduce the concrete resistivity by increasing the ion concentration in the pore solution, changing the pore structure, and reacting chemically with the concrete components [35,36].

The test results of concrete cracking time and maximum crack width indicate that the concrete cracking time significantly decreases with an increase in chloride ion concentration.

Moreover, under the condition of a constant total electric quantity, it further shortens as the current density increases. The specific test results are shown in Table 12.

Table 12. Cracking results of concrete cover layers for test specimens at different chloride ion concentrations.

Specimen Number	Cracking Time/h	Maximum Crack Width at Day 10/mm	Specimen Number	Concrete Cracking Time/h	Maximum Crack Width on Day 20/mm
D0-W1	No cracks	/	D0-W2	No cracks	/
D0.5-W1	No cracks	/	D0.5-W2	No cracks	/
D3.0-W1	No cracks	/	D3.0-W2	439	0.27
D5.0-W1	No cracks	/	D5.0-W2	386	0.21
D0-Z1	No cracks	/	D0-Z2	No cracks	/
D0.5-Z1	No cracks	/	D0.5-Z2	342	0.44
D3.0-Z1	231	0.03	D3.0-Z2	219	0.53
D5.0-Z1	192	0.37	D5.0-Z2	169	1.26
D0-Q1	No cracks	/	D0-Q2	No cracks	/
D0.5-Q1	213	0.05	D0.5-Q2	251	1.48
D3.0-Q1	218	0.05	D3.0-Q2	198	1.56
D5.0-Q1	121	0.97	D5.0-Q2	121	2.24

Under the condition of a constant total electric quantity, it decreases with an increase in current density. In the experimental group with a current density of 3.0 mA/cm^2, compared to the slightly corrosive environment, the concrete cracking times in the moderately corrosive and highly corrosive environments decreased by 48.75% and 52.62%, respectively. In the experimental group with a moderately corrosive environment, compared to a current density of 0.5 mA/cm^2, the concrete cracking times decreased by 34.21% and 47.22% under current densities of 3.0 mA/cm^2 and 5.0 mA/cm^2, respectively. This indicates that the cracking time of the concrete cover is significantly shortened under the synergistic effect of stray currents and chloride ions.

When there is no stray current interference in the environment, no cracking occurs in the reinforced concrete specimens under various chloride salt environments. However, even when the specimens are in a slightly corrosive environment, cracking occurs as the current density increases. This shows that under the action of a single factor, stray current corrosion has a greater impact on concrete cracking compared to chloride salt corrosion. Nevertheless, in environments with coupled stray currents and chloride salts, the promoting effect of an increase in environmental chloride ion concentration on concrete cracking is stronger than that of an increase in current density. This indicates that under coupled action, the chloride salt concentration has a more significant impact on concrete cracking [37].

Further data fitting was conducted to obtain a second-order polynomial that characterizes the change in concrete cracking time with current density and soil Cl^- concentration, as shown in Equation (4).

$$t_{cr} = 5.765 \times 10^2 - 4.584 \times 10 i_{corr} - 2.112 \times 10^{-1} C_{Cl^-} + 1.728 i_{corr}^2 + 2.190 \times 10^{-3} i_{corr} \times C_{Cl^-} + 2.789 \times 10^{-5} C_{Cl^-}^2 \quad (4)$$

where

tcr is the concrete cracking time, with the unit of h;

icorr is the current density, with the unit of mA/cm^2;

C_{Cl^-} is the soil Cl^- concentration, with the unit of mg/kg.

The coefficient of determination R^2 for the above fitting formula is 0.95, with a relative standard deviation of 8.44%, an average relative error of 7.68%, and a maximum absolute error of 44.98 h. The fitted surface is shown in Figure 15.

After the electromigration corrosion test was completed, the concrete specimens were split perpendicular to the chloride ion erosion surface. The $AgNO_3$ color development method test was carried out on the fractured section of the concrete after the specimens

were split. The chloride ion erosion depths of each specimen under different environmental factors after 10 d and 20 d are shown in Figure 16. For the electromigration specimens, the driving effect of the current significantly accelerated the transport of chloride ions in the concrete. Under the coupled action of stray currents and chloride salts, chloride ions reached the surface of the steel bars in most specimens at an early stage of the test. When using the $AgNO_3$ color development method to test the chloride ion erosion in concrete, obvious AgCl precipitates will form when the chloride ion concentration in the concrete pore solution reaches approximately 0.03 mol/L [38]. In addition, other anions (such as carbonate and sulfate ions) present in the concrete react with silver ions [39], interfering with the color development effect of chloride ions and thus affecting the detection accuracy. Moreover, a decrease in the OH^- concentration in carbonated concrete may lead to the failure of the color development reaction [39].

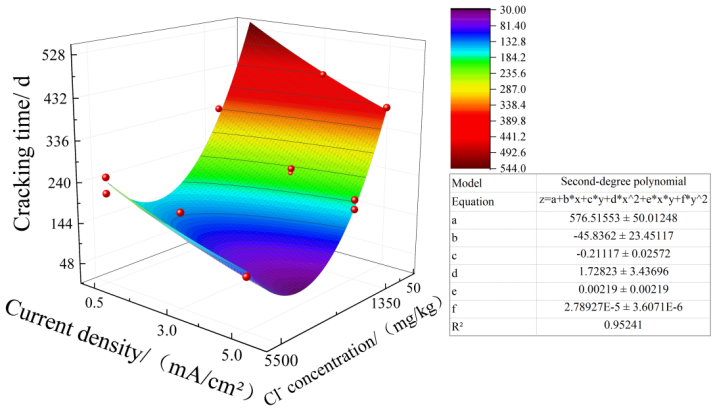

Figure 15. Fitted surface for concrete cracking time.

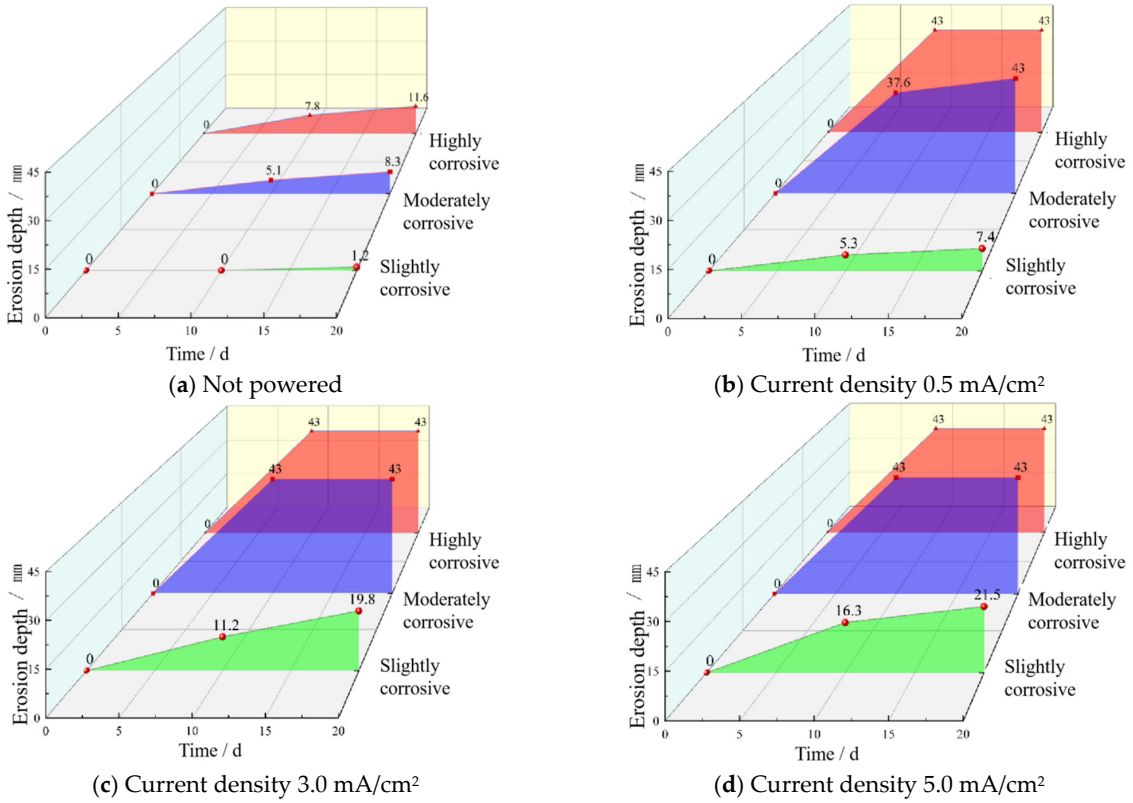

Figure 16. Depth of chloride ion erosion in concrete under different environmental factors. Note: Since the concrete specimen's protective layer thickness is 43 mm, a corrosion depth of 43 mm indicates that chloride ions have reached the reinforcement surface.

3.4. Analysis of Corrosion in Reinforcing Bars Under Coupling Effects

After the electromigration corrosion test, the concrete specimens were split using a 100 t electro-hydraulic servo universal testing machine and a multifunctional specimen splitting device. The corroded steel bars were removed, and their surfaces were cleaned of residual concrete and epoxy resin anti-corrosion layers using files and blades. The steel bars were then pickled, and the mass of each steel bar after corrosion was weighed using an electronic balance. Subsequently, the theoretical corrosion amount, measured corrosion amount, and measured corrosion rate of the steel bars in the concrete under different environmental factors were calculated. The corrosion rates of the steel bars under different current densities are shown in Figure 17.

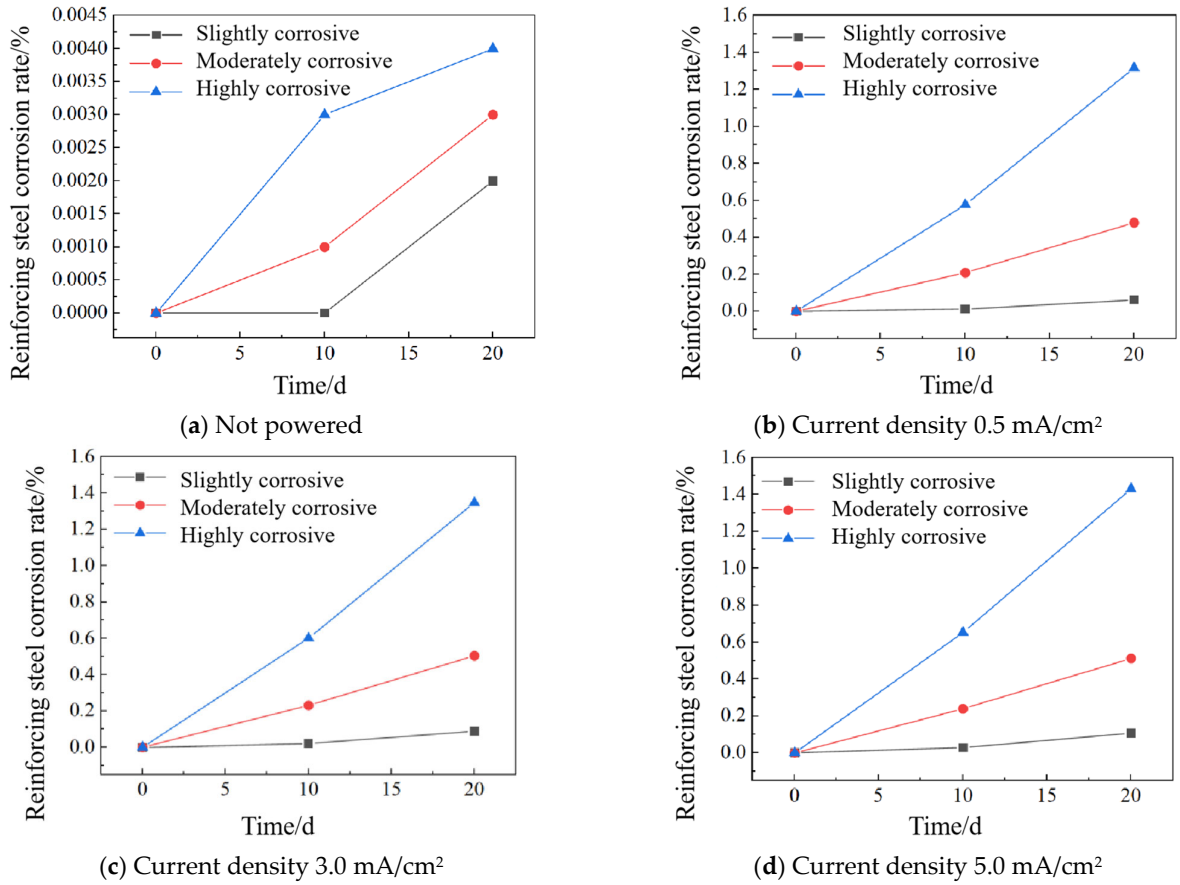

Figure 17. Corrosion rate of reinforcing bars under different environmental factors.

In the three chloride salt environments, the actual corrosion rates of the non-electrified groups (D0-x) after 10 d and 20 d were all below 0.004%. This indicates that when there is no direct-current stray current, steel bar corrosion is mainly triggered by the natural diffusion of chloride ions, and the corrosion rate is relatively slow. Even when the chloride ion concentration is as high as 5500 mg/kg, the steel bars hardly corrode within a short period (20 d).

Under electrified conditions, chloride ion concentration is the primary factor influencing the corrosion rate of steel bars. With consistent current density and electrification duration, an increase in chloride ion concentration leads to a significant rise in the corrosion rate. In an environment with a continuous current density of 0.5 mA/cm^2, as the chloride ion concentration rises from 50 mg/kg to 1350 mg/kg and 5500 mg/kg, the corrosion rate of steel bars after 10 days of electrification increases from 0.012% to 0.209% and 0.577%, respectively. After 20 days, the corrosion rate further rises from 0.062% to 0.480% and

1.317%, respectively. In highly corrosive environments, the average corrosion rate of steel bars is 2.75 times higher than in moderately corrosive environments, and several times higher than in slightly corrosive ones.

Under the condition of a constant total electric quantity, the influence of current density on the corrosion rate is relatively limited. In a highly corrosive environment, when the current density increases from 0.5 mA/cm^2 to 3.0 mA/cm^2 and 5.0 mA/cm^2, the corrosion rate of the steel bars after 10 d of electrification only rises from 0.577% to 0.602% and 0.652%, respectively. After 20 d of electrification, the corrosion rate only increases from 1.317% to 1.347% and 1.430%, respectively. With the increase in current density, the average corrosion rate of the steel bars only increases by approximately 3% and 10%.

The corrosion rate of steel bars increases as the concrete cracks. In a highly corrosive environment where the concrete cracks relatively early (the concrete in all electrified environments cracks before the tenth day), when the current density is 0.5 mA/cm^2, 3.0 mA/cm^2, and 5.0 mA/cm^2, the corrosion rates of the steel bars in the specimens during the first ten days are 80.7 mg/d, 83.8 mg/d, and 91.0 mg/d, respectively. After cracking, these rates increase to 102.6 mg/d, 105.0 mg/d, and 109.2 mg/d, respectively.

The actual corrosion rate is significantly lower than the theoretical rate. This is because the current in the electromigration test flows through the steel bars indirectly via the concrete cover, meaning the actual current passing through the steel bar surface is always less than the current entering the concrete. Additionally, only a portion of the current contributes to the dissolution of the steel bars, while a large amount may be involved in side reactions or limited by mass transfer [40,41]. In this experiment, the current efficiency (η) increases with both chloride ion concentration and current density. At a chloride ion concentration of 50 mg/kg and a current density of 0.5 mA/cm^2, η ranges from 0.3% to 0.8%. However, when the chloride ion concentration increases to 5500 mg/kg and the current density rises to 5.0 mA/cm^2, η reaches between 16.5% and 18.1%.

4. Conclusions

This study employed two experimental methods, namely electromigration and electrified corrosion, combined with means such as monitoring of concrete resistivity, determination of chloride ion erosion depth, and analysis of steel bar corrosion rate. It investigated the cracking rules of concrete cover, chloride ion transport characteristics, and steel bar corrosion behavior under different current densities and chloride salt concentrations. The influences of various factors on structural deterioration under coupled actions were clarified, and the following conclusions were drawn:

(1) This study systematically investigated the synergistic deterioration mechanism of reinforced concrete under the combined influence of chloride ions and stray direct current (DC) through accelerated corrosion experiments using both electromigration and impressed-current methods. The results revealed that chloride concentration primarily governs corrosion progression, while current density controls the corrosion rate. Their coupling significantly accelerates the cracking of the concrete cover. At a current density of 3.0 mA/cm^2, the cracking times in moderate and severe environments were reduced by 48.75% and 52.62%, respectively, compared to the mild condition. Under 0.5 mA/cm^2, the 20-day corrosion rate of steel bars in the severe environment (1.317%) was 2.75 times that in the moderate environment (0.480%). The proposed cracking-time prediction model achieved high accuracy (R^2 = 0.95, mean relative error = 7.68%), effectively reflecting the deterioration process under service conditions.

(2) Significant differences were observed between the two experimental methods. The electromigration specimens exhibited later cracking but deeper chloride penetration,

whereas the impressed-current specimens showed more pronounced strip-shaped pitting corrosion and an increased corrosion rate after cracking (from 80.7 mg/d to 102.6 mg/d at 0.5 mA/cm^2). These differences indicate that corrosion behavior is jointly controlled by electrochemical reaction mode and ion transport, highlighting the complementary mechanisms of the two methods.

(3) The variation in concrete resistivity demonstrated the staged nature of deterioration. Without stray current, resistivity decreased progressively with chloride diffusion. Under stray current, the resistivity of electromigration specimens first increased and then decreased, while that of impressed-current specimens first decreased and then stabilized, showing a slight rebound three to five days before cracking. This "rebound" phenomenon reflects the coupled influence of matrix dissolution and corrosion product accumulation, revealing the destructive effect of stray current on the microstructural continuity of concrete.

(4) The actual corrosion amount of steel was far below the theoretical Faraday value, indicating low current utilization efficiency. In mild environments (0.5 mA/cm^2), the efficiency was only 0.3–0.8%, increasing to 16.5–18.1% in severe environments (5.0 mA/cm^2). This demonstrates that chloride ions not only enhance current conduction but also accelerate anodic dissolution, significantly amplifying the corrosion effect.

(5) Compared with previous studies, this work uniquely quantifies the multifactor response behavior of reinforced concrete under the coupled influence of chloride and stray current, and proposes a combined electromigration–impressed-current testing system and a cracking-time prediction model. The integration of experimental data with the predictive framework represents a novel contribution. The findings deepen the scientific understanding of synergistic corrosion mechanisms and provide valuable engineering guidance for durability design and protection strategies of reinforced concrete structures in metro, coastal, and electrified railway environments.

(6) Based on the experimental results, several measures can be recommended to mitigate corrosion in existing reinforced concrete structures exposed to chloride and stray current coupling. Improving the electrical insulation between the structure and surrounding soil can effectively reduce stray current leakage. The application of cathodic protection systems and conductive coatings can help maintain the steel reinforcement in a passive state. In addition, the use of surface sealants or corrosion inhibitors can decrease chloride ingress, while increasing the concrete cover thickness and ensuring high concrete quality are essential to slow down the corrosion process. These practical strategies can enhance the durability and service life of reinforced concrete structures under complex electrochemical environments.

The findings of this study are closely related to practical durability issues in reinforced concrete structures. The combined effects of chloride ingress and stray direct current (DC) are among the key factors responsible for premature corrosion and cracking in metro tunnels, coastal defense systems, and electrified railway structures. The synergistic corrosion mechanism identified in this study, together with the developed predictive model for cracking time, provides a quantitative basis for service-life assessment, material selection, and protective design of reinforced concrete in complex electrochemical environments. The analysis of current efficiency deviation and its relationship with actual corrosion loss provides theoretical support for improving electrochemical acceleration methods and enhancing the accuracy of durability prediction, thereby strengthening the link between experimental research and engineering practice. Meanwhile, long-term field exposure tests are recommended to compare deterioration patterns between indoor accelerated and real-world conditions, enabling the correction of test parameters and the establishment of a

more accurate correlation model. Together, these efforts contribute to a more systematic and scientific framework for the full life-cycle protection of reinforced concrete structures.

Limitations and Future Work: It is important to note that this study was conducted under conditions without applied mechanical stress. In actual engineering structures, reinforced concrete members are often subjected to various stress levels due to service loads. Applied stress can induce microcracking within the concrete matrix, potentially accelerating the ingress of aggressive agents like chloride ions and altering the electrochemical response. Therefore, the corrosion rates and cracking times reported herein may be conservative compared to those in loaded structures. Future research should incorporate combined mechanical–electrochemical testing setups to investigate the coupling effects of stress, stray current, and chloride salts, which will lead to a more comprehensive and representative durability assessment model for practical applications.

Author Contributions: Conceptualization, Y.N. and W.Z.; methodology, Y.N.; software, Y.N.; validation, L.W.; formal analysis, Y.N.; investigation, Y.N. and L.W.; resources, W.Z.; writing—original draft preparation, Y.N. and W.Z.; visualization, Y.N.; supervision, W.Z.; project administration, W.Z.; funding acquisition, W.Z. All authors have read and agreed to the published version of the manuscript.

Funding: This research received no specific grant from any funding agency in the public, commercial, or not-for-profit sectors.

Data Availability Statement: The original contributions presented in this study are included in the article. Further inquiries can be directed to the corresponding author.

Conflicts of Interest: The author declares no conflicts of interest.

Appendix A. Chemical Composition of HPB300 Steel Reinforcement

Element	C	Mn	Si	P	S	Fe
Content (%)	0.17	1.33	0.42	0.020	0.018	98.042

References

1. Abadel, A.A. Experimental and numerical study on flexural enhancement of reinforced self-compacting concrete beams through various strengthening approaches. *Adv. Struct. Eng.* **2025**, *28*, 2463–2487. [CrossRef]
2. Qiao, Y.; Zhang, W.; Cheng, J.; Tong, L.; Sun, C.; Deng, J.; Ge, F. Experimental and Theoretical Investigations on the Bond–Slip Behavior of Newly Poured Concrete and Reinforcement Bars Under Traffic-Induced Vibrations in Bridge Widening. *Int. J. Concr. Struct. Mater.* **2025**, *19*, 84. [CrossRef]
3. Geng, M. A Practical Research based on Steel Fiber Reinforced Concrete Construction Technology in Road and Bridge Engineering. *J. World Archit.* **2025**, *9*, 43–49. [CrossRef]
4. Xavier, L.; Liliya, S. *Reinforced Concrete from 1906 to Today: Application to the Evaluation of Structures in the Framework of an Asset Management of Civil Engineering Works*; John Wiley & Sons, Inc.: Hoboken, NJ, USA, 2025. [CrossRef]
5. Wang, X.; Huang, P.; Yuan, Y.; Wang, D.; Yang, Y.; Liu, X. Chloride Diffusion and Corrosion Assessment in Cracked Marine Concrete Bridges Using Extracted Crack Morphologies. *Buildings* **2025**, *15*, 3214. [CrossRef]
6. Yang, J.; Han, S.; Cao, Q.; Zhao, X.; Yu, X.; Liu, J. The Dynamic Mechanical Properties of High Strength and High Ductility Concrete Under a Corrosion Environment. *Buildings* **2025**, *15*, 2983. [CrossRef]
7. Miao, Z.; Liu, Y.; Chen, K.; Niu, X.; Hogan, L.; Lu, Y. A practical approach to determining mechanical degradation of corroded steel bars considering the corrosion environment conditions. *Constr. Build. Mater.* **2025**, *487*, 142090. [CrossRef]
8. Lapiro, I.; Eid, R.; Kovler, K. Passive protection of reinforced concrete columns against stray currents and chloride attack. *Constr. Build. Mater.* **2025**, *472*, 140814. [CrossRef]
9. Zhu, W.; Ren, Y.; Tang, F.; Xu, Y.; Yu, L.; Xu, Y. Morphology of Corrosion Pits Induced by Stray Current and Chloride in RC Transportation Infrastructure. *J. Mater. Civ. Eng.* **2025**, *37*, 04025136. [CrossRef]
10. Reiser, M.; Kouřil, M.; Forcellese, P.; Bellezze, T. Application of Resistometric Sensors in Investigation of Zinc Corrosion in Simulated Concrete Environments. *Buildings* **2025**, *15*, 635. [CrossRef]

11. Liu, W.; Xiao, J.; Li, Y.; Guo, Z.; Liu, H. Study on stray current corrosion behavior of rebars in cement mortar by XCT nondestructive testing method. *Constr. Build. Mater.* **2025**, *464*, 140136. [CrossRef]
12. Wang, Z.; Liu, Y.; Ye, K.; Chen, S.; Yang, G. Mechanistic Understanding of the Non-Uniform Corrosion of Steel Bridges: From the Perspective of Micro-Environments. *Buildings* **2025**, *15*, 422. [CrossRef]
13. Lee, T.; Kim, D.; Cho, S.; Kim, M.O. Advancements in Surface Coatings and Inspection Technologies for Extending the Service Life of Concrete Structures in Marine Environments: A Critical Review. *Buildings* **2025**, *15*, 304. [CrossRef]
14. Moreno-Herrera, J.; Vega-Juarez, N.; Varela-Rivera, J.; Fernandez-Baqueiro, L.; Castro-Borges, P. The Effect of Steel Reinforcement Diameter on the Behavior of Concrete Beams with Corrosion. *Buildings* **2025**, *15*, 266. [CrossRef]
15. Sannasiraj, R.D.A.; Shi, S.; Liu, X.; Gryllias, K.; Vandepitte, D.; Chronopoulos, D.; Zhang, L. A fully coupled depth-dependent corrosion model for reinforced concrete piles under marine environmental conditions. *Constr. Build. Mater.* **2025**, *472*, 140795. [CrossRef]
16. Wang, S.; Cao, J.; Gong, F.; Peng, Y.; Wang, Z.; Zhao, Y.; Zeng, B. Insights on the multiple ions distribution in concrete under stray current: From experiments to multi-field simulation. *J. Build. Eng.* **2024**, *98*, 111502. [CrossRef]
17. Liu, H.; Yang, L.; Kang, K.; Gao, D.; Liu, G.; Zhang, Y.; Zhang, Y. Mechanical properties and corrosion mechanism of steel fiber reinforced concrete (SFRC) subjected to stray current. *J. Build. Eng.* **2024**, *96*, 110519. [CrossRef]
18. Zhang, Y.; Zhang, X.; Jin, F.; Zhao, X. Impact of Stone Powder Content on Corrosion Resistance in Reinforced Concrete Under Stray Current and Chloride Interactions. *Materials* **2023**, *17*, 196. [CrossRef]
19. Gao, Y.; Yu, H.; Ma, H.; Feng, T.; Xu, M.; Song, S.; Li, L. Electrochemical characters of chloride induced reinforcement corrosion in concrete structures: Initial pitting criterion and the law of mass transfer resistance of concrete cover. *Structures* **2025**, *74*, 108635. [CrossRef]
20. Evangelatos, A.; Schaber, B.; Galler, R. Streustromkorrosion von Stahlfaserbeton. *BHM Berg- und Hüttenmännische Monatshefte* **2024**, *169*, 649–653. [CrossRef]
21. *GB/T 1499.1-2008*; Steel for the Reinforcement of Concrete—Part 1: Hot Rolled Plain Bars. China Standards Press: Beijing, China, 2008.
22. *GB/T 27690-2023*; Silica Fume for Mortar and Concrete. China Standards Press: Beijing, China, 2023.
23. *GB/T 1596-2017*; Fly Ash for Use in Cement and Concrete. China Standards Press: Beijing, China, 2017.
24. *GB/T 228.1-2021*; Metallic Materials—Tensile Testing—Part 1: Test Methods at Room Temperature. China Standards Press: Beijing, China, 2021.
25. *GB/T 50082-2024*; Standard Test Methods for Long-Term Performance and Durability of Normal Concrete. China Architecture & Building Press: Beijing, China, 2024.
26. Liu, Q.; Yuan, M.; Zhang, J.; Qiang, S. Research on the corrosion inhibition effect of xanthium sibiricum on reinforced steel and the prediction of reinforced concrete performance under a stray current and chloride environment. *Appl. Sci.* **2024**, *14*, 6986. [CrossRef]
27. Chen, Y.; Chen, M.; Chen, R.; Kang, X. Deterioration mechanism of chloride attack on reinforced concrete under stray current and high hydraulic pressure coexistence environment. *Mater. Struct.* **2023**, *56*, 160. [CrossRef]
28. Lee, D.; Jeong, A.J. Study on the interference effect of electric hybrid cathodic protection system on steel and concrete piles. *J. Adv. Mar. Eng. Technol. (JAMET)* **2023**, *47*, 325–330. [CrossRef]
29. Otsuki, N.; Nagataki, S.; Nakashita, K. Evaluation of $AgNO_3$ solution spray method for measurement of chloride penetration into hardened cementitious matrix materials. *Mater. J.* **1992**, *89*, 587–592. [CrossRef]
30. Akduman, S.; Öztürk, H. Effect of reinforcement corrosion on structural behavior in reinforced concrete structures according to initiation and propagation periods. *Buildings* **2024**, *14*, 4026. [CrossRef]
31. Wei, H.; Wan, H.; Yuan, S.; Liu, G.; Teng, J.; Shi, N.; Liu, Z. A new gelling material: Properties of recycled aggregate concrete under conditions of complete cement replacement using steel slag, ore slag, and fly ash. *Constr. Build. Mater.* **2025**, *464*, 140180. [CrossRef]
32. Han, M.; Li, J. Enhancement of Compressive Strength and Durability of Sulfate-Attacked Concrete. *Buildings* **2024**, *14*, 2187. [CrossRef]
33. Liu, H.; Li, K.; Li, Y.; Liu, S.; Dong, Z.; Cui, H.; Liu, W. Corrosion behavior of steel fiber reinforced concrete under ambipolar stray current interference. *Constr. Build. Mater.* **2024**, *411*, 134302. [CrossRef]
34. Wei, L.; Liu, J.; Shu, H.; Cui, Q.; Peng, W.; Gong, H.; Xue, Y.; Han, M. Degradation Characteristics and Mechanisms of Steel Fiber-Reinforced Concrete Linings in Subsea Tunnels: Insights from Accelerated Erosion Tests with Applied Electric Fields. *J. Mar. Sci. Eng.* **2025**, *13*, 670. [CrossRef]
35. Xu, Y.; Yuan, Q.; De Schutter, G.; Wang, F.; Li, H. Detecting the damage of concrete subjected to fatigue load coupled with freeze-thaw cycles using alternating current electric impedance spectroscopy. *Cem. Concr. Compos.* **2023**, *142*, 105224. [CrossRef]
36. Wei, H.; Wan, H.; Gao, L.; Liu, G.; Yuan, S.; Zhou, K.; Teng, J.; Shi, N.; Liu, Z. All-solid-waste concrete with novel gelling particles solid-loaded with bacteria: Mechanical properties and crack repair prediction. *Constr. Build. Mater.* **2025**, *484*, 141853. [CrossRef]

37. Shirole, D.; Volpatti, G.; Guerini, A.; Zampini, D.; Cusatis, G.; Loria, A.F.R. Effects of electrodeposition in concrete mediated by electric currents of variable polarity. *Cem. Concr. Res.* **2023**, *172*, 107254. [CrossRef]
38. Kim, M.Y.; Yang, E.I.; Yi, S.T. Application of the colorimetric method to chloride diffusion evaluation in concrete structures. *Constr. Build. Mater.* **2013**, *41*, 239–245. [CrossRef]
39. Pontes, C.V.; Réus, G.C.; Araújo, E.C.; Medeiros, M.H.F. Silver nitrate colorimetric method to detect chloride penetration in carbonated concrete: How to prevent false positives. *J. Build. Eng.* **2021**, *34*, 101860. [CrossRef]
40. Behforouz, B.; Moghbel Esfahani, S.; Tavakoli, D. Prediction of Electrical Resistivity of Concrete Containing Electric Arc Furnace Slag as Fine Aggregate Using Gene Expression Programming Method. *Buildings* **2025**, *15*, 806. [CrossRef]
41. Yu, X.; Li, S.; Zheng, J.; Chang, X.; Liao, Y.; Chen, D. Degradation process of reinforced concrete under chloride and sulfate attack with and without electric field. *J. Build. Eng.* **2023**, *78*, 107588. [CrossRef]